

Quasi-one-dimensional structure and possible helical antiferromagnetism of RbMn_6Bi_5

Long Chen,^{1,2,#} Linlin Zhao,^{1,2,#} Xiaole Qiu,^{3,#} Qinghua Zhang,¹ Kai Liu,³ Qisheng Lin,^{4,5,} Gang Wang^{1,6,7,*}*

¹ Beijing National Laboratory for Condensed Matter Physics, Institute of Physics, Chinese Academy of Sciences, Beijing 100190, China

² University of Chinese Academy of Sciences, Beijing 100049, China

³ Department of Physics and Beijing Key Laboratory of Opto-electronic Functional Materials & Micro-nano Devices, Renmin University of China, Beijing 100872, China

⁴ Ames Laboratory, U.S. Department of Energy, Ames, IA 50011, USA

⁵ Department of Chemistry, Iowa State University, Ames, IA 50011, USA

⁶ School of Physical Sciences, University of Chinese Academy of Sciences, Beijing 100049, China

⁷ Songshan Lake Materials Laboratory, Dongguan, Guangdong 523808, China

ABSTRACT: Quasi-one-dimensional materials exhibit not only unique crystal structure but also abundant physical properties such as charge density wave, Luttinger liquid, and superconductivity. Here we report the discovery, structure, and physical properties of a new manganese-based quasi-one-dimensional material RbMn_6Bi_5 , which crystallizes in a monoclinic space group $C2/m$ (No. 12) with lattice parameters $a = 23.286(5) \text{ \AA}$, $b = 4.6215(9) \text{ \AA}$, $c = 13.631(3) \text{ \AA}$, and $\beta = 125.00(3)^\circ$. The structure features $[\text{Mn}_6\text{Bi}_5]^{-1}$ double-walled column extending along the $[010]$ direction, together with Bi-Bi homoatomic bonds linking the columns and the counter cation Rb^+ . The temperature-dependent resistivity clearly indicates a significant resistivity anisotropy for RbMn_6Bi_5 , whereas the magnetic susceptibility and specific heat measurements

show that RbMn_6Bi_5 is antiferromagnetic below 82 K. The density functional theory calculations indicate that RbMn_6Bi_5 is a quasi-one-dimensional metal with possible helical antiferromagnetic configuration. The discovery of RbMn_6Bi_5 confirms the viability of discovering new quasi-one-dimensional material in manganese-based compounds.

INTRODUCTION

Manganese-based materials have attracted much attention for their various crystal structures and novel physical properties. MnP is the first manganese-based superconductor by suppressing the helical magnetic order using high pressures.^{1,2} Mn_2O_3 is the first example of spin-induced multiferroic binary oxide having the unusual perovskite structure with the same atoms occupying both A and B sites.³ The perovskite manganite TbMnO_3 is a magnetic ferroelectric material which exhibits gigantic magnetoelectric and magnetocapacitance effects.⁴ The perovskite manganite $\text{La}_{1-x}\text{M}_x\text{MnO}_3$ ($M = \text{Ca}, \text{Sr}, \text{Ba}$ and so on) have been extensively investigated due to their colossal magnetoresistance (CMR) and potential application in magnetic recording.⁵ The perovskite manganite also shows magnetocaloric effect arising from significant entropy change.^{6,7} In fact, many manganese-based materials show significant entropy change, exhibiting various applications. For example, the Fe_2P -type $\text{MnFeP}_{0.45}\text{As}_{0.55}$ is an attractive candidate for commercial magnetic refrigerator⁸, which is promising to largely reduce the usage of greenhouse gases like hydrofluorocarbons (HFCs) in the future sustainable technologies.⁹

For quasi-two-dimensional (Q2D) manganese-based materials, the antiferromagnetic (AFM) EuMnBi_2 exhibits magnetically confined two-dimensional Dirac fermions and a bulk half-integer quantum Hall effect.¹⁰ The Q2D AFM MnBi_2Te_4 has attracted attention for its realization of quantum anomaly hall effect (QAHE)^{11,12} and its tunability of magnetism combined with topological properties through magnetic fields or layer constructions¹³⁻¹⁵. The Q2D manganese pnictides have received special attention as they are potential parent compounds for superconductivity. Among them,

both the ZrCuSiAs-type $\text{LaMn}Pn\text{O}$ and the ThCr_2Si_2 -type BaMn_2Pn_2 ($Pn = \text{P, As, Sb, and Bi}$) compounds are AFM materials.¹⁶⁻²³ Interestingly, $(\text{Ca/Sr})\text{Mn}_2Pn_2$ ($Pn = \text{P, As, Sb, and Bi}$) compounds with the trigonal CaAl_2Si_2 -type structure also exhibit AFM character.^{20, 24-28} It should be mentioned that the structure of SrMn_2P_2 transits from the trigonal CaAl_2Si_2 -type to the body-centered tetragonal ThCr_2Si_2 -type structure under pressure.²⁹ Mn-doped SrFe_2As_2 has also shown a structural evolution from tetragonal ($P4/nmm$) to trigonal ($P-3m1$) with a possible intrinsic Griffiths phase and a large miscibility gap.³⁰ Other Q2D manganese-based materials that exhibit antiferromagnetism at different temperatures were also reported, such as ZnMn_2O_4 , $\text{Sr}_2\text{Mn}_3\text{Sb}_2\text{O}_2$ and $\text{BaMnO}_2\text{Ag}_2\text{Se}_2$.³¹⁻³³

As to quasi-one-dimensional (Q1D) materials, referring to those structures that consist of one-dimensional atomic chain or column-like motifs, abundant physical properties can arise from such unique structures, e.g., charge density wave,³⁴ the Luttinger liquid behavior,³⁵ and superconductivity.³⁶⁻³⁸ Linear chain systems containing $[\text{MnCl}_3]^-$,^{39,40} $[\text{MnCl}_4]^{2-}$,⁴¹ $[\text{MnX}_2]^{2-}$ ($X = \text{S, Se and Te}$)⁴² or edge-shared MnX_6 octahedra ($X = \text{S and Se}$)⁴³⁻⁴⁵ have been extensively used as model systems for studying properties of one-dimensional exchange-coupled systems. Exploration and synthesis of Mn-based Q1D materials are highly desired for their unique crystal structures and exotic properties. Recently, a manganese-based Q1D material KMn_6Bi_5 consisting of unique $[\text{Mn}_6\text{Bi}_5]^-$ columns has been reported.⁴⁶ In this structure, the magnetic Mn-centered Mn_5 column are separated by nonmagnetic Bi_5 tunnels. This structural type provides an exciting model for Q1D magnetic materials.

In this work, we tried to replace K in KMn_6Bi_5 by the larger sized Rb atoms with aim to study the influence of size factor and its transport properties. Herein, we report the synthesis, crystal structure, magnetism, electronic transport, and density functional theory (DFT) calculations of RbMn_6Bi_5 obtained by the solution growth method. RbMn_6Bi_5 exhibits an AFM ordering at 82 K and obvious resistivity anisotropy. DFT calculations indicate that RbMn_6Bi_5 has a possible helical AFM order. Compared to KMn_6Bi_5 , the title compound shows weaker interchain coupling.

EXPERIMENTAL AND CALCULATION METHODS

Single crystal growth. RbMn₆Bi₅ single crystals were grown by a high temperature solution growth method. Rb chunk (99.75%, Alfa Aesar), Mn powder (99.95%, Alfa Aesar), and Bi granules (99.999%, Sinopharm) were used as the starting materials. The starting materials in a molar ratio of Rb : Mn : Bi = 1 : 4 : 8 were put into an alumina crucible and then vacuum sealed in a silica ampoule. All manipulations were carried out in an argon-filled glovebox. The ampoule was heated to 973 K over 15 h, held at the temperature for 8 h, and then slowly cooled down to 773 K at a rate of 2.4 K/h. At 773 K, the single crystals with size up to 5 mm × 0.5 mm × 0.5 mm were separated from the remaining liquids by centrifuging the ampoule. Then the ampoule was opened in the argon-filled glovebox. The obtained single crystals are shiny-silver needles and air-sensitive, so specimen preparation for property measurements were handled in glovebox.

Structure and composition characterization. Single crystal X-ray diffraction data of RbMn₆Bi₅ were collected using Bruker D8 VENTURE with Mo K α radiation ($\lambda = 0.71073\text{\AA}$). The structure was solved by a direct method and refined by the full-matrix method based on F^2 using the SHELXTL software package.⁴⁷ The high-angle annular-dark-field (HAADF) images were conducted on an ARM-200F (JEOL) scanning transmission electron microscopy (STEM) operated at 200 kV with a CEOS Cs corrector (CEOS GmbH) to cope with the probe forming objective spherical aberration. The attainable resolution of the probe defined by the objective pre-field is 78 picometers.

Physical property measurements. Magnetization and resistivity measurements were carried out using a physical property measurement system (PPMS) (Quantum Design, QD). Magnetic susceptibility was measured with applied magnetic fields parallel and perpendicular to the rod ([010] direction) using the zero-field-cooling (ZFC) and field-cooling (FC) protocols. For the ZFC protocol, sample was first cooled down to 10 K without an applied magnetic field, data were collected with an applied magnetic field during the heating process. In contrast, for the FC protocol, a magnetic field was

applied during sample cooling, and data were collected under the same applied magnetic field during the process of warming up. Magnetization hysteresis loops at 5 K, 50 K, 100 K, 200 K, and 300 K were measured under the applied magnetic field up to 8 T parallel and perpendicular to the rod ([010] direction). The resistivity was measured by QD PPMS under the standard four-probe configuration, with the applied current (about 2 mA) parallel or perpendicular to the rod ([010] direction), whereas the magnetic field always being perpendicular to the rod ([010] direction). Heat capacity measurement was also carried out in QD PPMS below 200 K. To protect the samples from air and water, thin film of N-type grease was spread to cover the sample.

DFT calculations. The DFT calculations were carried out with the projector augmented wave (PAW) method as implemented in the Vienna *ab initio* simulation Package (VASP).⁴⁸⁻⁵⁰ The generalized gradient approximation (GGA) of the Perdew-Burke-Ernzerhof (PBE) type was adopted for the exchange-correlation function.^{51,52} The cutoff energy of the plane-wave basis was 520 eV and the energy convergence standard was set to 10^{-6} eV. The $4 \times 4 \times 4$ and $2 \times 10 \times 4$ Monkhorst-Pack K-point meshes were employed for the Brillouin zone (BZ) sampling of the unit cell and the conventional cell, respectively. The experimental crystal data were adopted to perform static calculations on RbMn_6Bi_5 , taking into account both the collinear and the non-collinear magnetic configurations with the spin-orbit coupling (SOC). Parallel calculations without SOC were also conducted, which yield an increase of 4.9 meV/Mn in the stable energy state. So the calculation results with SOC are discussed in the following session.

RESULTS AND DISCUSSION

1. Structure

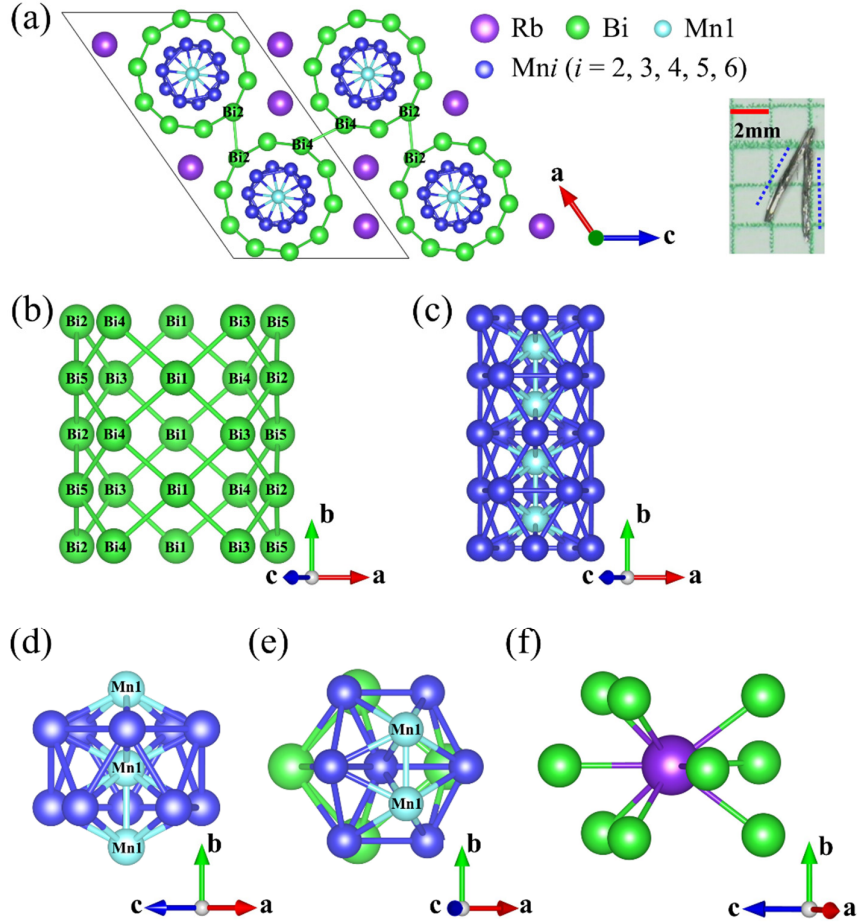


Figure 1. (a) The crystal structure of RbMn_6Bi_5 viewed along b -axis, only Bi-Bi and Mn-Mn bonds are marked for clarity. The inset shows an optical photograph of the as-grown needle-like crystals. The dotted lines donate the rod directions. (b) A Bi_5 tunnel defined by Bi-Bi bonds. (c) A Mn_5 tunnel defined by Mn-Mn bonds (blue), together with one-dimensional Mn1-Mn1-Mn1 chain in the center (cyan). (d) The Mn1-centered Mn_{12} icosahedral cluster. (e) The coordination environment of Mn_i ($i = 2, 3, 4, 5,$ and 6). (f) The coordination environment of Rb.

Table 1. Crystal data and structure refinement for RbMn_6Bi_5 .

Empirical formula	RbMn_6Bi_5
CCDC number	2064508
Formula weight	1460.01 g/mol
Space group / Z	$C2/m$ (No. 12) / 4
Unit cell dimensions	$a = 23.286(5) \text{ \AA}$ $\alpha = 90^\circ$ $b = 4.6215(9) \text{ \AA}$ $\beta = 125.00(3)^\circ$

Volume / d_{cal}	$c = 13.631(3) \text{ \AA}$ $\gamma = 90^\circ$
Reflections collected/R(int)	$1201.6(6) \text{ \AA}^3 / 8.070 \text{ g/cm}^3$
Data / restraints / parameters	8926 / 0.0696
Goodness-of-fit on F^2	1691 / 0 / 73
Final R indices [$I > 2\sigma(I)$]	1.074
R indices (all data)	$R1 = 0.0644, wR2 = 0.1751$
Largest diff. peak and hole	$R1 = 0.0697, wR2 = 0.1793$
	5.635 and $-4.895 \text{ e.\AA}^{-3}$

Table 2. Atomic coordinates and equivalent isotropic displacement parameters for RbMn_6Bi_5 .

Atom	<i>Wyck.</i>	<i>Site symm.</i>	<i>x/a</i>	<i>y/b</i>	<i>z/c</i>	$U(\text{eq})(\text{\AA}^2)$
Rb	<i>4i</i>	<i>m</i>	0.1307(2)	0	-0.1165(3)	0.039(1)
Bi1	<i>4i</i>	<i>m</i>	0.1351(1)	0.5000	0.1121(1)	0.028(1)
Bi2	<i>4i</i>	<i>m</i>	0.4059(1)	-0.5000	0.4200(1)	0.027(1)
Bi3	<i>4i</i>	<i>m</i>	0.2780(1)	0	0.2138(1)	0.027(1)
Bi4	<i>4i</i>	<i>m</i>	0.0427(1)	0	0.1638(1)	0.029(1)
Bi5	<i>4i</i>	<i>m</i>	0.4738(1)	-1.0000	0.6562(1)	0.027(1)
Mn1	<i>4f</i>	<i>l</i>	0.2500	-0.7500	0.5000	0.017(1)
Mn2	<i>4i</i>	<i>m</i>	0.3704(2)	-0.5000	0.5833(4)	0.020(1)
Mn3	<i>4i</i>	<i>m</i>	0.3337(2)	-1.0000	0.4565(4)	0.019(1)
Mn4	<i>4i</i>	<i>m</i>	0.1894(2)	0	0.2909(4)	0.021(1)
Mn5	<i>4i</i>	<i>m</i>	0.1385(2)	0.5000	0.3199(4)	0.018(1)
Mn6	<i>4i</i>	<i>m</i>	0.2637(2)	0.5000	0.3425(4)	0.019(1)

The crystal structure data of RbMn_6Bi_5 determined from single crystal X-ray diffraction are given in Table 1, Table 2 and Table S1. RbMn_6Bi_5 shares a same structure motif as that of KMn_6Bi_5 ,⁴⁶ which is also monoclinic with $C2/m$ (No. 12) space group. The structure of RbMn_6Bi_5 , Figure 1 (a)-(c), features $[\text{Mn}_6\text{Bi}_5]^{-1}$ columns extending along the $[010]$ direction, whereas the counter cation Rb^+ ions surround $[\text{Mn}_6\text{Bi}_5]^{-1}$

columns acting as separators. Each $[\text{Mn}_6\text{Bi}_5]^{-1}$ column consists of three substructures from the center to out: the one-dimensional Mn1-Mn1-Mn1 atomic chain in the center, the Mn₅ tunnel built with Mn2, Mn3, Mn4, Mn5, and Mn6, and the outmost Bi₅ tunnel. Both Mn₅ and Bi₅ tunnels are built from face-shared pentagonal antiprisms. The center of Mn₁₀ pentagonal antiprism is occupied by Mn1, resulting in a formation of Mn1@Mn₁₂ icosahedral cluster (Figure 1d). The Mn-Mn bond lengths (Table S1) in the Mn₅ column range from 2.3108(5) Å to 2.773(6) Å, comparable to those (2.3 - 2.8 Å) of KMn₆Bi₅.⁴⁶ The Mn₅ and Bi₅ columns are interconnected through Mn-Bi bonds (Figure 1e) ranging from 2.783(5) Å to 3.065(3) Å, also close to those (2.8 - 3.0 Å) in KMn₆Bi₅.⁴⁶ The Bi-Bi bond lengths within Bi₅ columns range from 3.493(1) Å (Bi1-Bi4) to 3.611(2) Å (Bi1-Bi3), similar to those in KMn₆Bi₅.⁴⁶ However, the two inter-column Bi-Bi separations, 3.606(1) Å (Bi2-Bi2) and 3.703(4) Å (Bi4-Bi4), are both ~ 0.4 Å longer than those of KMn₆Bi₅ [3.5687(12) Å and 3.6517(13) Å],⁴⁶ arising from the size factor of counter cations. Rb atoms are located at the 4i (*x*, 0, *z*) Wyckoff sites, each surrounded by nine Bi atoms with Rb-Bi separations of 3.707(4) Å - 3.912(3) Å (Figure 1f).

RbMn₆Bi₅ can be regarded as a Zintl phase, and an oxidation state of 2.33 for Mn can be calculated following the Zintl concept.⁵³ In other words, the electron configuration of Mn atoms can be written as [Ar]3d^{4.67}. Considering the itinerant nature of electrons in a metallic compound (below) and the Mn-Mn covalent bonding character, the [Ar]3d^{4.67} configurations, though, does not necessarily mean a 2:1 mixture of d⁵ and d⁴ configurations despite that different environments of Mn1 and Mni (*i* = 2-5) atoms could be argued.

Compared to those of KMn₆Bi₅,⁴⁶ the cell parameters of RbMn₆Bi₅ (cf. Table 1) are slightly expanded, with *a* increased by 1.3%, *b* increased by 0.2%, *c* increased by 1.9%, and β increased by 0.3%. The expansions in *a* and *c* are about an order of magnitude larger than that of *b*. Such expansions appear to be correlated with the larger intercolumn Bi-Bi bonds resulted by the substitution of Rb⁺ for K⁺, which weakens the intercolumn interactions. Similar variations of intra- and inter-chain distances have

been reported for the Q1D superconducting materials $\text{K}_2\text{Cr}_3\text{As}_3$, $\text{Rb}_2\text{Cr}_3\text{As}_3$, and $\text{Cs}_2\text{Cr}_3\text{As}_3$ containing $[\text{Cr}_3\text{As}_3]^{2-}$ atomic chain.^{37,54,55} The spherical aberration-corrected transmission electron microscopy analysis on RbMn_6Bi_5 single crystal shown in Figure S1 illustrates that the interplanar spacings for $(0\bar{2}0)$, $(1\bar{1}\bar{2})$, and (204) are 2.16 Å, 3.06 Å, and 2.24 Å, respectively, consistent with the XRD results.

2. Magnetic susceptibility

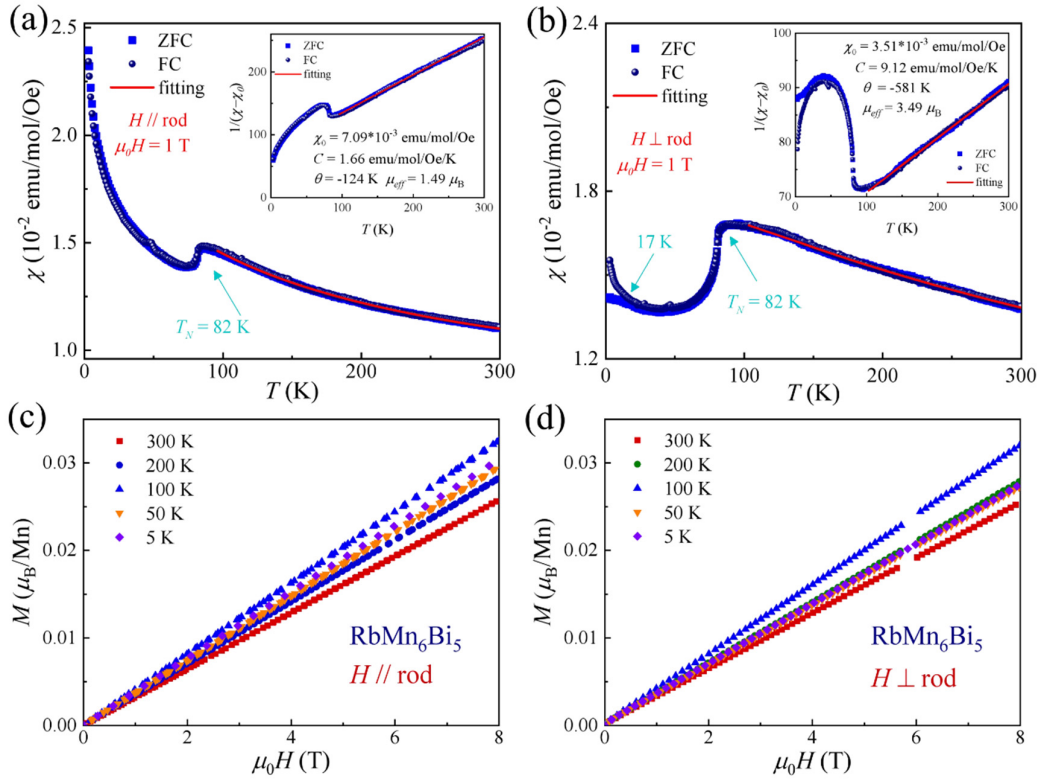


Figure 2. The temperature dependence of magnetic susceptibility for RbMn_6Bi_5 single crystal measured under a magnetic field of 1 T for (a) $H // \text{rod}$ and (b) $H \perp \text{rod}$ ([010] direction) under ZFC and FC measurements. Red lines show the linear fittings by Curie-Weiss law at the high temperature region from 150 K to 300 K. The field dependence of magnetizations with (c) $H // \text{rod}$ and (d) $H \perp \text{rod}$ at different temperatures.

The ZFC and FC magnetic susceptibility of RbMn₆Bi₅ single crystal under 1 T with applied magnetic fields parallel and perpendicular to the rod ([010] direction) are shown in Figures 2(a) and 2(b), respectively. Both plots show a cusp at about 82 K, which separates the regions of paramagnetic and AFM phases, respectively. For the high temperature region, the magnetic susceptibility follows the Curie-Weiss law, $\chi = \chi_0 + \frac{C}{T-\theta}$, where χ_0 is the temperature-independent contribution including the diamagnetic contribution of the orbital magnetic moment and the Pauli paramagnetic contribution of conduction electron, C is the Curie constant and θ is the Curie temperature.⁵⁶ The fitted values are $\chi_0 = 7.09 \times 10^{-3} \text{ emu mol}^{-1} \text{ Oe}^{-1}$, $\theta = -124 \text{ K}$, and $C = 1.66 \text{ emu mol}^{-1} \text{ Oe}^{-1} \text{ K}^{-1}$ for $H // \text{rod}$ ([010] direction), whereas $\chi_0 = 3.51 \times 10^{-3} \text{ emu mol}^{-1} \text{ Oe}^{-1}$, $\theta = -581 \text{ K}$, and $C = 9.12 \text{ emu mol}^{-1} \text{ Oe}^{-1} \text{ K}^{-1}$ for $H \perp \text{rod}$. Negative θ indicate that the interactions in both directions are of AFM characters. Interestingly, the difference between ZFC and FC data are quite small for $H // \text{rod}$ (Figure 2(a)). In contrast, FC curve and ZFC curve bifurcate clearly at 17 K for magnetic field perpendicular to the rod (Figure 2(b)). FC/ZFC bifurcation is commonly seen for intermetallic compounds featuring like anisotropic structures⁵⁷ or complex clusters.⁵⁸⁻⁶⁰ For an AFM system, a ratio of $|\theta/T_N|$ suggests the extent of magnetic frustration. In general, a heavily frustrated magnet has a ratio larger than 10, and a moderately frustrated magnet has a ratio within 1-10.⁶¹⁻⁶³ In this case, the ratio of $|\theta/T_N|$ is estimated to be 1.51 for $H // \text{rod}$ and 7.09 for $H \perp \text{rod}$, indicating a moderately frustrated system. This is reasonable considering the geometry of the building unit of Mn1-centered Mn₁₂ icosahedron (Figure 1d).^{64,65}

Following the equation $\mu_{eff} = \sqrt{\frac{8C}{n}}$, where n is the number of magnetic atoms, the effective moment $\mu_{eff} = 1.81 \mu_B/\text{Mn}$ and $3.49 \mu_B/\text{Mn}$ can be derived for $H // \text{rod}$ and $H \perp \text{rod}$, respectively. As former mentioned, the average oxidation state of Mn is about 2.33, corresponding to an electronic configuration of $d^{4.67}$. The experimental μ_{eff} values fall, as expected, in the range of the spin-only magnetic moment of low-spin $t_{2g}^{4.67}$ ($1.38 \mu_B$) and high-spin $t_{2g}^3 e_g^{1.67}$ ($5.48 \mu_B$) of octahedrally coordinated $d^{4.67}$. The large difference for μ_{eff} in the two perpendicular directions signals a strong magnetic

anisotropy, consistent with the one-dimensional structural motif (Figure 1). However, the magnetic anisotropy in KMn_6Bi_5 is much weaker ($1.56 \mu_B$ for $H \parallel ab$ versus $1.37 \mu_B$ for $H \perp ab$)⁴⁶, indicating that the size factor plays a key role. Figures 2(c) and 2(d) show the magnetization of RbMn_6Bi_5 under applied magnetic fields parallel and perpendicular to the rod ([010] direction), respectively. Both magnetizations increase linearly with magnetic field ranging from 5 K to 300 K and remains unsaturated up to 8 T, and no hysteresis loop has been observed in both directions. This absence of hysteresis in M - H curves at all temperatures confirms the dominant AFM interactions at low temperatures, same as in KMn_6Bi_5 .⁴⁶

3. Resistivity

Within the measuring temperature range, the resistivity of RbMn_6Bi_5 in [010] direction, shown in Figure 3(a), decreases with decreasing temperature and shows an anomaly at 81 K. The transition at 81 K coincides with the AFM transition temperature observed in the magnetic susceptibility measurements, and is direction-independent [Figure 2(b) and 3(d)] and sample-independent (Figure S2). The room-temperature resistivity for RbMn_6Bi_5 is estimated to be $0.44 \text{ m}\Omega \text{ cm}$ in the [010] direction, smaller than the maximum value ($1 \text{ m}\Omega \text{ cm}$) determined by the MIR limit.⁵⁶ The residual resistivity ratio $\text{RRR} = \frac{\rho(300 \text{ K})}{\rho(2 \text{ K})} = 18.46$ indicates that the crystalline quality of RbMn_6Bi_5 is high. Above 81 K, the resistivity is slowly saturated and can be fitted (Figure 3(a)) using the formula $\frac{1}{\rho(T)} = \frac{1}{\rho_{\text{sat}}} + \frac{1}{\rho_{\text{ideal}}}$, where ρ_{sat} represents the saturation resistivity, ρ_{ideal} is the ideal resistivity that satisfies the Boltzmann equation. ρ_{ideal} is proportional to the temperature in the high temperature region and can be described by $\rho_{\text{ideal}} = \rho_r + aT$.⁶⁶ The fitting yields $\rho_{\text{sat}} = 0.51 \text{ m}\Omega \text{ cm}$, $\rho_r = 0.18 \text{ m}\Omega \text{ cm}$, and $a = 0.01 \text{ m}\Omega \text{ cm K}^{-1}$. Below 81 K, the resistivity can be well fitted using $\rho = \rho_0 + AT^\alpha$, with fitted parameters $\rho_0 = 0.022 \text{ m}\Omega \text{ cm}$, $A = 3.67 \times 10^{-4} \text{ m}\Omega \text{ cm K}^{-1.90}$, and $\alpha = 1.90$. The value of power is close to 2, suggesting that the resistivity of RbMn_6Bi_5 satisfies the Fermi liquid behavior at low temperature. The magnetoresistance of RbMn_6Bi_5 , following the

formula $\frac{\rho(H)-\rho(0)}{\rho(0)}$, is extrapolated to be 165% at 2 K under a magnetic field of 8 T and electric current parallel to the rod.

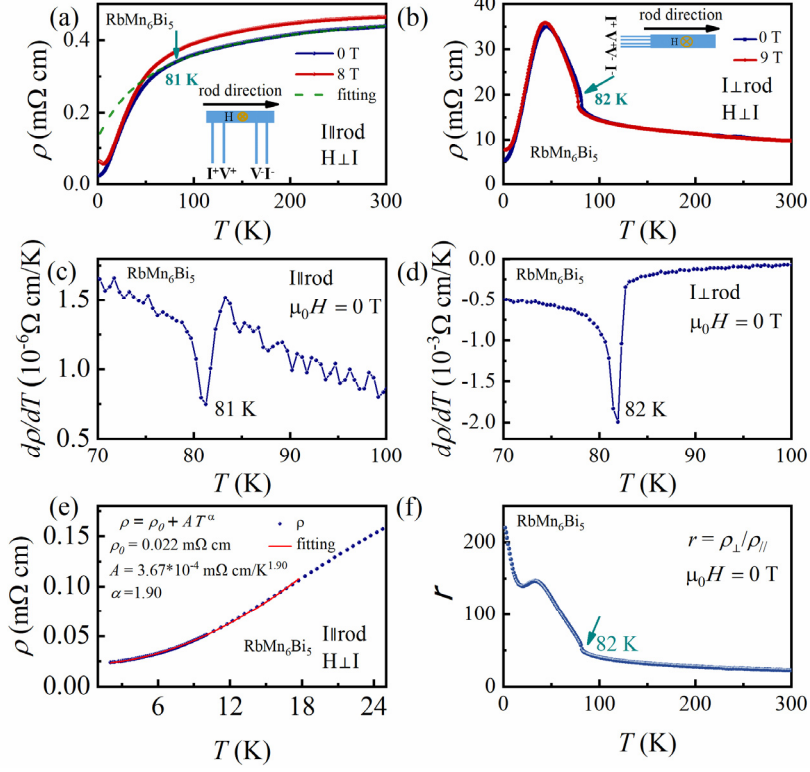


Figure 3. The temperature dependence of resistivity $\rho(T)$ for RbMn₆Bi₅ single crystal measured with electric current (a) parallel to and (b) perpendicular to the rod ([010] direction) for measurements w/o applied magnetic field, and (c)-(d), their respective 1st derivatives in range of 70 K-100 K. (e) The enlargement of low-temperature resistivity with electric current parallel to the rod at 0 T. (f) The temperature dependence of anisotropic resistivity ratio for RbMn₆Bi₅ measured without magnetic field.

In comparison, the temperature dependence of resistivity with applied electric current perpendicular to the rod, Figure 3(b), increases rapidly with the increasing temperature before reaching a maximum at 44 K, and then decreases rapidly till to Neel temperature ($T_N = 82$ K) as shown in Figure 3(d). Similar transition was observed for KMn₆Bi₅ and its origin was usually attributed to a dimensional crossover of electrons in low-dimensional materials.^{46,67} The ratio of resistivity in two directions, or the resistivity

anisotropy, as shown in Figure 3(f), decreases with the increasing temperature, with staging effect occur at the magnetic transition temperature ($T_N = 82$ K). The saturated value of the resistivity anisotropy at low temperature is about 240, much larger than that of KMn_6Bi_5 (~ 20),⁴⁶ indicating a larger anisotropy, same as the magnetic anisotropy. Considering the AFM ordering, the increase of resistivity with the decreasing temperature below 82 K should be resulted from the superzone gap effect.^{68,69}

4. Specific heat

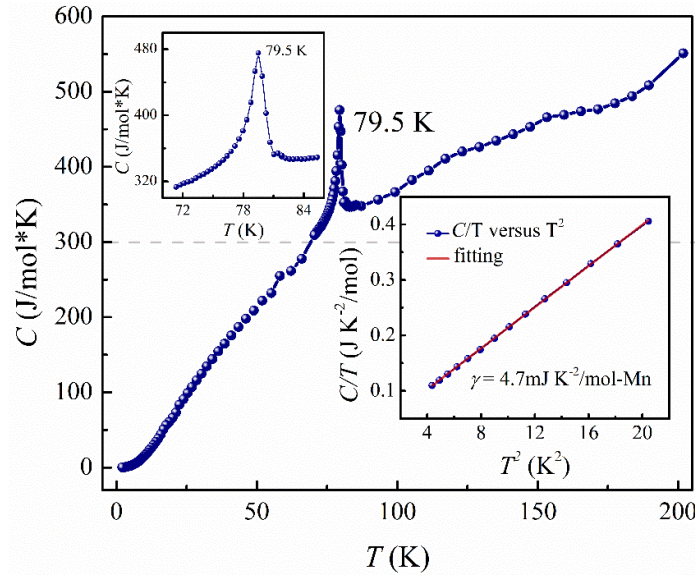


Figure 4. The temperature dependence of specific heat for RbMn_6Bi_5 single crystal. The upper inset shows the enlargement of specific heat around 79.5 K. The lower inset shows the $C(T)/T$ versus T^2 , the red solid line is the linear fitting by using Debye model $C/T = \gamma + \beta T^2$.

Figure 4 shows the temperature dependence of specific heat for RbMn_6Bi_5 single crystal from 2.2 K to 200 K. The specific heat shows a sharp peak at 79.5 K with a big jump $\Delta C \approx 175 \text{ J mol}^{-1} \text{ K}^{-1}$, close to the transition temperatures of magnetic susceptibility (82 K) and resistivity (81 K) attributed to the AFM transition. The specific heat exceeds Dulong–Petit limit ($3NR \sim 300 \text{ J/mol}\cdot\text{K}$) at high temperature because the phonon contribution of N-type grease used for protecting the sample is more prominent

at higher temperature, as also observed for KMn_6Bi_5 .⁴⁶ In contrast, N-type grease does not affect the Sommerfeld coefficient of RbMn_6Bi_5 at low temperature because of its insulating character. The specific heat below 4.5 K can be well fitted (see lower inset) with the Debye model $C/T = \gamma + \beta T^2$, where γ is the Sommerfeld coefficient and is proportional to the density of states at the Fermi level. In the formula $C/T = \gamma + \beta T^2$, that is $C = \gamma T + \beta T^3$, γT represents the contribution from the electron, whereas βT^3 represents the contribution of the lattice. And the Debye temperature Θ_D can be calculated by $(12\pi^4 R n / 5\beta)^{1/3}$, where R represents the molar gas constant and n is the number of atoms in the chemical formula. The fitted parameters are $\gamma = 28.2 \text{ mJ K}^{-2}$ per formula [$4.7 \text{ mJ K}^{-2} (\text{mol-Mn})^{-1}$], $\beta = 18.54 \text{ mJ K}^{-4} \text{ mol}^{-1}$, and $\Theta_D = 107.8 \text{ K}$. The Sommerfeld coefficient of RbMn_6Bi_5 is smaller than that of KMn_6Bi_5 [$39(1) \text{ mJ K}^{-2}$ per formula].⁴⁶ The observation of materials with bigger alkali metal ions having smaller Sommerfeld coefficients is also held for Q1D materials $\text{Rb}_2\text{Cr}_3\text{As}_3$ ⁵⁴ and $\text{K}_2\text{Cr}_3\text{As}_3$ ³⁷, but the reason remains to be uncovered.

5. Electronic structure

As shown in Figure 1, each unit cell of RbMn_6Bi_5 consists of two columns made of Mn1-centered Mn_{12} icosahedra, one at $(1/4, y, 1/2)$ and another at $(3/4, y, 1/2)$. Viewed along the $[010]$ direction, the two pentagons of an icosahedron with different y values are rotated by $\sim 36^\circ$. For clarification, these two pentagons are differentiated by size in Figure 5, which shows 11 typical magnetic configurations we have considered in this work. Among these 11 configurations, eight (1-8) are collinear and the other three (9-11) are non-collinear magnetic models. The energy differences between each magnetic configuration and the nonmagnetic (NM) state [$\Delta E = (E_{\text{total}} - E_{\text{NM}}) / N_{\text{Mn}}$] are calculated to evaluate the magnetic ground state. As shown in Table 3, model 11 has the lowest total energy, followed by models 9 and 6. The spins in these models are antiparallel either in ac plane (model 6) and or along the b axis (models 9 and 11). Particularly for model 11, spins on the two different pentagons (with different y) in the same Mn column form opposite vortex and those for the central Mn1 atoms also have opposite spin

polarizations, sign of a possible helical magnetic order.

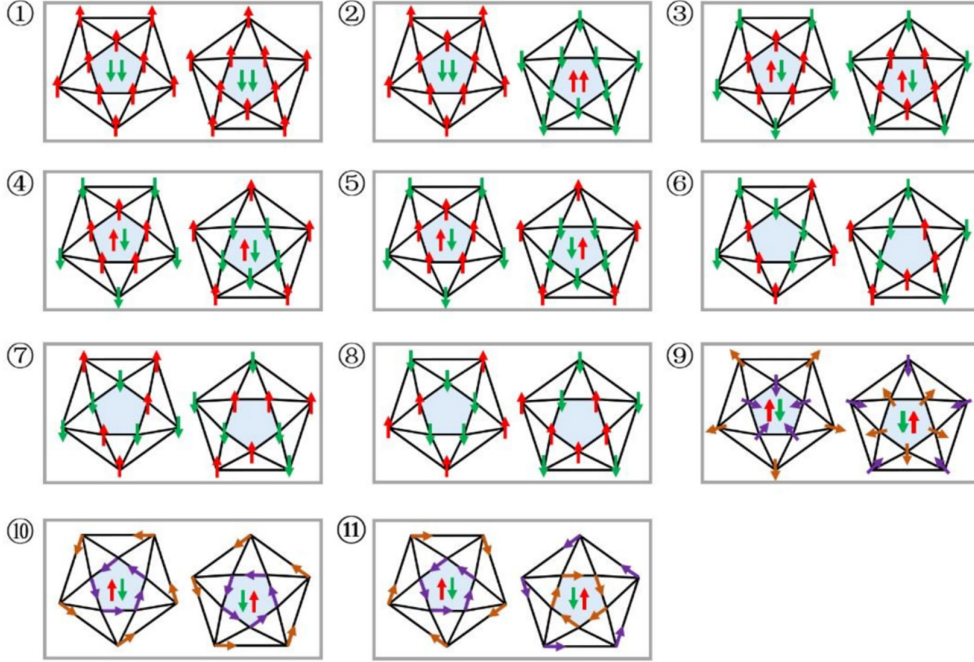


Figure 5. Schematic diagrams of eleven magnetic configurations for RbMn_6Bi_5 . The conventional cell is used for clarity. Arrows denote the directions of magnetic moments. Pentagons with different sizes represent the five Mn atoms with different y coordinates. The two arrows at the center of pentagons represent Mn1 atoms in the core of Mn column with different y . Note the zero moment for Mn1 atoms in configurations 6 - 8 after spin-polarized relaxation.

Table 3. Relative energies of different magnetic configurations for RbMn_6Bi_5 with respect to that of the NM state.

Magnetic Structure	1	2	3	4	5	
ΔE (meV/Mn)	-308.4	-304.2	-300.0	-303.1	-303.0	
Magnetic Structure	6	7	8	9	10	11
ΔE (meV/Mn)	-336.2	-310.4	-305.4	-341.8	-317.8	-350.0

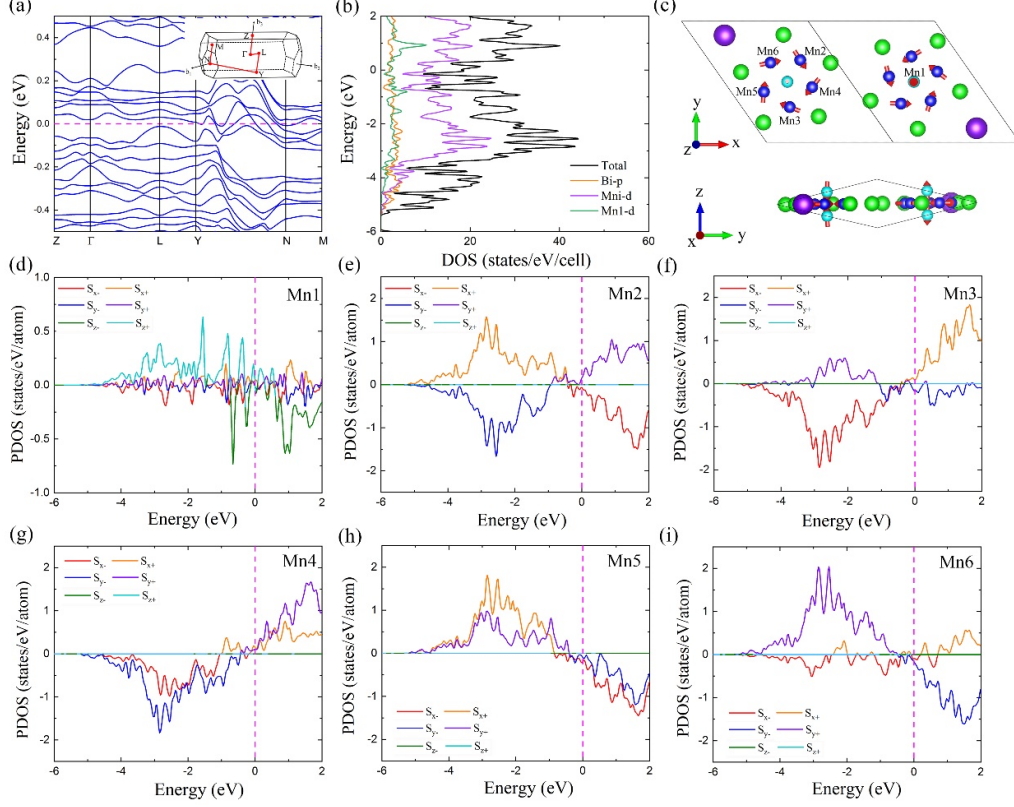


Figure 6. (a) Band structure with SOC near the Fermi level (purple dash line) of RbMn₆Bi₅. The inset shows the first Brillouin zone (BZ). (b) DOS (total and partial) for model 11. (c) Calculated magnetic moments of Mn atoms in model 11. (d)-(i) Spin-resolved 3d partial DOS with SOC of Mni ($i = 1 - 6$) atoms.

To further understand the origin of helical AFM configuration (model 11 in Figure 5), the band structure, DOS, and corresponding spin-resolved DOS of RbMn₆Bi₅ are calculated. As shown in Figure 6 (a), the band dispersions along the Z- Γ -L-Y and N-M paths are fairly flat, typical for Q1D structural motif. There are several bands crossing the Fermi energy, indicating that RbMn₆Bi₅ is a metal, consistent with experimental data. The DOS near the Fermi level are mainly contributed by the Mn 3d states, Figure 6(b), which spread from c.a. -5.0 eV up to 3.0 eV. The integrated areas for Mn1 and the average of Mni ($i = 2 - 6$) DOSs up to the Fermi level are close, 5.22 versus 5.03, meaning that all Mn atoms have similar numbers of 3d electrons filling the valence bands. The spin polarization leads to a splitting between the majority and minority spin

states that can be projected separately along the three orthogonal directions (S_x , S_y , S_z). According to our calculations, the spin-resolved DOS for Mn1 are heavily populated by S_{z^+} and S_{z^-} states at Fermi energy (Figure 6(d)), whereas those for Mni ($i = 2, 3, 4, 5$, and 6) atoms, S_x and S_y contributions are dominant, as shown in Figure 6(e) - (i). This suggests an interesting picture about the overall behavior of magnetic spins: the magnetic moment of Mn1 is almost aligned along S_z direction and the magnetic moments of Mni ($i = 2, 3, 4, 5$, and 6) are confined in S_x - S_y plane. Such a scenario yields a helical AFM configuration shown in Figure 6(c). As can be seen, the spins of nearest neighboring Mn1 atoms are oppositely aligned in the chain direction, whereas those of Mni atoms are confined in the pentagonal plane in a helical mode. The calculated local moments for Mni atoms in the pentagon are about $2.9 \mu_B/\text{cell}$, and that for the central Mn1 atom is about $0.6 \mu_B/\text{cell}$, consistent with the relative change of μ_{eff} calculated from experimental data (above). The total magnetic moment is small, $0.02 \mu_B/\text{cell}$, common for AFM materials. All these factors lead us to tentatively believe that RbMn_6Bi_5 is a moderately frustrated magnet with helical AFM interaction. Further effort, such as neutron diffraction, will be needed to characterize the magnetic structure of the title compound.

CONCLUSION

In summary, we have successfully synthesized a new manganese-based Q1D material RbMn_6Bi_5 , which contains $[\text{Mn}_6\text{Bi}_5]^{-1}$ double-walled columns along the $[010]$ direction. The lattice parameters a and c are slightly increased compared with those of KMn_6Bi_5 . The magnetic susceptibility, resistivity, and specific heat measurements show an ordering with AFM character at about 82 K. Temperature-dependent resistivity reveals that RbMn_6Bi_5 is a metal with strong resistivity anisotropy. Both magnetic susceptibility and resistivity shows a significant anisotropy compared with KMn_6Bi_5 , which may be related to the substitution of a larger size cation Rb^+ for K^+ . The first-principles calculations reveal a possible helical AFM magnet with Q1D metallic electronic structure. Further investigation through replacing Rb^+ with other alkali metal ions (Li^+ , Na^+ and Cs^+), alkaline earth metal ions (Ca^{2+} , Sr^{2+} and Ba^{2+}) or organic

cations (like NH_4^+ and CH_3NH_3^+) could give more insights into the interplay of size factor and transport properties.

Supporting Information

Table S1 lists the selected environments and interatomic distances for RbMn_6Bi_5 . Figure S1 shows the FFT SAED pattern and HAADF image of RbMn_6Bi_5 taking along the $[20\bar{1}]$ axis. Figure S2 displays the temperature dependence of resistivity $\rho(T)$ for more RbMn_6Bi_5 single crystals.

Accession Codes

CCDC 2064508 contains the supplementary crystallographic data for this paper. These data can be obtained free of charge via www.ccdc.cam.ac.uk/data_request/cif, or by emailing data_request@ccdc.cam.ac.uk, or by contacting The Cambridge Crystallographic Data Centre, 12 Union Road, Cambridge CB2 1EZ, UK; fax: +44 1223 336033.

AUTHOR INFORMATION

Corresponding Authors

*qslin2009@gmail.com

*gangwang@iphy.ac.cn

Notes

The authors declare no competing financial interest.

ACKNOWLEDGEMENTS

L. Chen, L. L. Zhao, and X. L. Qiu contributed equally to this work. L. Chen, L. L. Zhao, and G. Wang acknowledge Prof. X. L. Chen of the Institute of Physics, Chinese Academy of Sciences for discussion. This work was partially supported by the National Natural Science Foundation of China (Grant Nos. 51832010, 51532010, 51572291, and

11774424), the National Key Research and Development Program of China (Grant Nos. 2018YFE0202600 and 2017YFA0302900), the Key Research Program of Frontier Sciences, Chinese Academy of Sciences (Grant No. QYZDJ-SSW-SLH013), and the Beijing Natural Science Foundation (Grant No. Z200005). Computational resources were provided by the Physical Laboratory of High Performance Computing at Renmin University of China. The work done by Q. S. Lin was supported by Ames Laboratory, U.S. DOE. Ames Laboratory is operated for the U.S. Department of Energy by Iowa State University under Contract No. DE-AC02-07CH11358.

REFERENCES

- (1) Cheng, J. G.; Matsubayashi, K.; Wu, W.; Sun, J. P.; Lin, F. K.; Luo, J. L.; Uwatoko, Y. Pressure induced superconductivity on the border of magnetic order in MnP. *Phys. Rev. Lett.* **2015**, *114*, 117001.
- (2) Matsuda, M.; Ye, F.; Dissanayake, S. E.; Cheng, J. G.; Chi, S.; Ma, J.; Zhou, H. D.; Yan, J. Q.; Kasamatsu, S.; Sugino, O.; Kato, T.; Matsubayashi, K.; Okada, T.; Uwatoko, Y. Pressure dependence of the magnetic ground states in MnP. *Phys. Rev. B.* **2016**, *93*, 100405(R).
- (3) Cong, J.; Zhai, K.; Chai, Y.; Shang, D.; Khalyavin, D. D.; Johnson, R. D.; Kozlenko, D. P.; Kichanov, S. E.; Abakumov, A. M.; Tsirlin, A. A.; Dubrovinsky, L.; Xu, X.; Sheng, Z.; Ovsyannikov, S. V.; Sun, Y. Spin-induced multiferroicity in the binary perovskite manganite Mn₂O₃. *Nat. Commun.* **2018**, *9*, 2996.
- (4) Kimura, T.; Goto, T.; Shintani, H.; Ishizaka, K.; Arima, T.; Tokura, Y. Magnetic control of ferroelectric polarization. *Nature.* **2003**, *426*, 55-58.
- (5) Ramirez, A. P. Colossal magnetoresistance. *J. Phys. Condens.: Matter.* **1997**, *9*, 8171–8199.
- (6) Zhang, X. X.; Tejada, J.; Xin, Y.; Sun, G. F.; Wong, K. W.; Bohigas, X. Magnetocaloric effect in La_{0.67}Ca_{0.33}MnO_δ and La_{0.60}Y_{0.07}Ca_{0.33}MnO_δ bulk materials. *Appl. Phys. Lett.* **1996**, *69*, 3596-3598.
- (7) Szewczyk, A.; Gutowska, M.; Piotrowski, K.; Dąbrowski, B. Direct and specific heat study of magnetocaloric effect in La_{0.845}Sr_{0.155}MnO₃. *J. Appl. Phys.* **2003**, *94*, 1873-

1876.

(8) Tegus, O.; Brück, E.; Buschow, K. H. J.; Boer, F. R. d. Transition-metal-based magnetic refrigerants for room-temperature applications. *Nature*. **2002**, *415*, 150-152.

(9) Cheng, H. Future earth and sustainable developments. *The Innovation*. **2020**, *1*, 100055.

(10) Masuda, H.; Sakai, H.; Tokunaga, M.; Yamasaki, Y.; Miyake, A.; Shiogai, J.; Nakamura, S.; Awaji, S.; Tsukazaki, A.; Nakao, H.; Murakami, Y.; Arima, T.-h.; Tokura, Y.; Ishiwata, S. Quantum Hall effect in a bulk antiferromagnet EuMnBi_2 with magnetically confined two-dimensional Dirac fermions. *Sci. Adv.* **2016**, *2*, e1501117.

(11) Otrokov, M. M.; Menshchikova, T. V.; Vergniory, M. G.; Rusinov, I. P.; Vyazovskaya, A. Y.; Koroteev, Y. M.; Bihlmayer, G.; Ernst, A.; Echenique, P. M.; Arnau, A.; Chulkov, E. V. Highly-ordered wide bandgap materials for quantized anomalous Hall and magnetoelectric effects. *2D Mater.* **2017**, *4*, 025082.

(12) Li, J. H.; Wang, C.; Zhang, Z. T.; Gu, B. L.; Duan, W. H.; Xu, Y. Magnetically controllable topological quantum phase transitions in the antiferromagnetic topological insulator MnBi_2Te_4 . *Phys. Rev. B*. **2019**, *100*, 121103(R).

(13) Otrokov, M. M.; Rusinov, I. P.; Blanco-Rey, M.; Hoffmann, M.; Vyazovskaya, A. Y.; Ereemeev, S. V.; Ernst, A.; Echenique, P. M.; Arnau, A.; Chulkov, E. V. Unique thickness-dependent properties of the van der Waals interlayer antiferromagnet MnBi_2Te_4 films. *Phys. Rev. Lett.* **2019**, *122*, 107202.

(14) Liu, C.; Wang, Y. C.; Li, H.; Wu, Y.; Li, Y. X.; Li, J. H.; He, K.; Xu, Y.; Zhang, J. S.; Wang, Y. Y. Robust axion insulator and Chern insulator phases in a two-dimensional antiferromagnetic topological insulator. *Nat. Mater.* **2020**, *19*, 522-527.

(15) Wang, P. Y.; Ge, J.; Li, J. H.; Liu, Y. Z.; Xu, Y.; Wang, J. Intrinsic magnetic topological insulators. *The Innovation*. **2021**, *2*, 100098.

(16) Yanagi, H.; Watanabe, T.; Kodama, K.; Iikubo, S.; Shamoto, S. i.; Kamiya, T.; Hirano, M.; Hosono, H. Antiferromagnetic bipolar semiconductor LaMnPO with ZrCuSiAs -type structure. *J. Appl. Phys.* **2009**, *105*, 093916.

(17) Emery, N.; Wildman, E. J.; Skakle, J. M.; Girit, G.; Smith, R. I.; McLaughlin,

A. C. Giant magnetoresistance in oxypnictides (La,Nd)OMnAs. *Chem. Commun.* **2010**, 46, 6777-6779.

(18) Emery, N.; Wildman, E. J.; Skakle, J. M. S.; McLaughlin, A. C.; Smith, R. I.; Fitch, A. N. Variable temperature study of the crystal and magnetic structures of the giant magnetoresistant materials LMnAsO (L=La, Nd). *Phys. Rev. B.* **2011**, 83, 144429.

(19) Zhang, Q.; Kumar, C. M. N.; Tian, W.; Dennis, K. W.; Goldman, A. I.; Vaknin, D. Structure and magnetic properties of LnMnSbO (Ln=La and Ce). *Phys. Rev. B.* **2016**, 93, 094413.

(20) Brock, S. L.; J. E. Greedan; S. M. Kauzlarich. Resistivity and Magnetism of AMn₂P₂ (A = Sr, Ba): The effect of structure type on physical properties. *J. Solid State Chem.* **1994**, 113, 303-311.

(21) An, J.; Sefat, A. S.; Singh, D. J.; Du, M. H. Electronic structure and magnetism in BaMn₂As₂ and BaMn₂Sb₂. *Phys. Rev. B.* **2009**, 79, 075120.

(22) Singh, Y.; Green, M. A.; Huang, Q.; Kreyssig, A.; McQueeney, R. J.; Johnston, D. C.; Goldman, A. I. Magnetic order in BaMn₂As₂ from neutron diffraction measurements. *Phys. Rev. B.* **2009**, 80, 100403.

(23) Saporov, B.; Sefat, A. S. Crystals, magnetic and electronic properties of a new ThCr₂Si₂-type BaMn₂Bi₂ and K-doped compositions. *J. Solid State Chem.* **2013**, 204, 32-39.

(24) Wang, Z. W.; Yang, H. X.; Tian, H. F.; Shi, H. L.; Lu, J. B.; Qin, Y. B.; Wang, Z.; Li, J. Q. Structural and physical properties of SrMn₂As₂. *J. Phys. Chem. Solids.* **2011**, 72, 457-459.

(25) Sangeetha, N. S.; Pandey, A.; Benson, Z. A.; Johnston, D. C. Strong magnetic correlations to 900 K in single crystals of the trigonal antiferromagnetic insulators SrMn₂As₂ and CaMn₂As₂. *Phys. Rev. B.* **2016**, 94, 094417.

(26) Bridges, C. A.; Krishnamurthy, V. V.; Poulton, S.; Paranthaman, M. P.; Sales, B. C.; Myers, C.; Bobev, S. Magnetic order in CaMn₂Sb₂ studied via powder neutron diffraction. *J. Magn. Magn. Mater.* **2009**, 321, 3653-3657.

(27) Bobev, S.; Merz, J.; Lima, A.; Fritsch, V.; Thompson, J. D.; Sarrao, J. L.; Gillissen,

M.; Dronskowski, R. Unusual Mn-Mn spin coupling in the polar intermetallic compounds CaMn_2Sb_2 and SrMn_2Sb_2 . *Inorg. Chem.* **2006**, *45*, 4047-4054.

(28) Gibson, Q. D.; Wu, H.; Liang, T.; Ali, M. N.; Ong, N. P.; Huang, Q.; Cava, R. J. Magnetic and electronic properties of CaMn_2Bi_2 : A possible hybridization gap semiconductor. *Phys. Rev. B.* **2015**, *91*, 085128.

(29) Xie, W.; Winiarski, M. J.; Klimczuk, T.; Cava, R. J. A tetragonal polymorph of SrMn_2P_2 made under high pressure – theory and experiment in harmony. *Dalton Trans.* **2017**, *46*, 6835-6838.

(30) Chen, L.; Cao, C.; Chen, H. X.; Guo, J. G.; Ma, J.; Hu, J. P.; Wang, G. Miscibility gap and possible intrinsic Griffiths phase in $\text{Sr}(\text{Fe}_{1-x}\text{Mn}_x)_2\text{As}_2$ crystals grown by transition metal arsenide flux. *Phys. Rev. B.* **2021**, *103*, 134509.

(31) Li, H.; Song, B.; Wang, W. J.; Chen, X. L. Facile synthesis, thermal, magnetic, Raman characterizations of spinel structure ZnMn_2O_4 . *Mater. Chem. Phys.* **2011**, *130*, 39-44.

(32) Jin, S. F.; Chen, X. L.; Guo, J. G.; Lei, M.; Lin, J. J.; Xi, J. G.; Wang W. J.; Wang, W. Y. $\text{Sr}_2\text{Mn}_3\text{Sb}_2\text{O}_2$ type oxyselenides: Structures, magnetism, and electronic properties of $\text{Sr}_2\text{AO}_2\text{M}_2\text{Se}_2$ (A = Co, Mn; M = Cu, Ag). *Inorg. Chem.* **2012**, *51*, 10185-10192.

(33) Zhou, T. T.; Wang, Y. M.; Jin, S. F.; Li, D. D.; Lai, X. F.; Ying, T. P.; Zhang, H.; Shen, S. J.; Wang, W. J.; Chen, X. L. Structures and physical properties of layered oxyselenides $\text{Ba}_2\text{MO}_2\text{Ag}_2\text{Se}_2$ (M = Co, Mn). *Inorg. Chem.* **2014**, *53*, 4154-4160

(34) Grüner, G. The dynamics of charge-density waves. *Rev. Mod. Phys.* **1988**, *60*, 1129-1181.

(35) Voit, J. One-dimensional Fermi liquids. *Rep. Prog. Phys.* **1994**, *57*, 977-1116.

(36) Takahashi, H.; Sugimoto, A.; Nambu, Y.; Yamauchi, T.; Hirata, Y.; Kawakami, T.; Avdeev, M.; Matsubayashi, K.; Du, F.; Kawashima, C.; Soeda, H.; Nakano, S.; Uwatoko, Y.; Ueda, Y.; Sato, T. J.; Ohgushi, K. Pressure-induced superconductivity in the iron-based ladder material BaFe_2S_3 . *Nat. Mater.* **2015**, *14*, 1008-1012.

(37) Bao, J. K.; Liu, J. Y.; Ma, C.-W.; Meng, Z. H.; Tang, Z. T.; Sun, Y. L.; Zhai, H. F.; Jiang, H.; Bai, H.; Feng, C. M.; Xu, Z. A.; Cao, G. H. Superconductivity in quasi-

one-dimensional $\text{K}_2\text{Cr}_3\text{As}_3$ with significant electron correlations. *Phys. Rev. X* **2015**, *5*, 011013.

(38) Mu, Q. G.; Ruan, B. B.; Zhao, K.; Pan, B. J.; Liu, T.; Shan, L.; Chen, G. F.; Ren, Z. A. Superconductivity at 10.4 K in a novel quasi-one-dimensional ternary molybdenum pnictide $\text{K}_2\text{Mo}_3\text{As}_3$. *Sci. Bull.* **2018**, *63*, 952-956.

(39) Skalyo, J.; Shirane, G.; Friedberg, S.A.; Kobayashi, H. Neutron scattering in linear chain antiferromagnet $\text{CsMnCl}_3 \cdot 2\text{H}_2\text{O}$, *Physical Review B*. **1970**, *2*, 1310-1317.

(40) Tancharakorn, S.; Fabbiani, F. P. A.; Allan, D. R.; Kamenev, K. V.; Robertson, N. Combined magnetic and single-crystal X-ray structural study of the linear chain antiferromagnet $(\text{CH}_3)_4\text{NMnCl}_3$ under varying pressure. *J. Am. Chem. Soc.* **2006**, *128*, 9205-9210.

(41) Munninghoff, G.; Treutmann, W.; Hellner, E.; Heger, G.; Reinen, D. Structure and Jahn-Teller effect in mixed-crystals $\text{Rb}_2\text{Cr}_{1-x}\text{Mn}_x\text{Cl}_4$ - A single-crystal neutron-diffraction study and spectroscopic results. *J. Solid State Chem.* **1980**, *34*, 289-299.

(42) Bronger, W.; Balkhardtdegen, H.; Schmitz, D. On alkali-metal manganese chalcogenides A_2MnX_2 with $\text{A} = \text{K}, \text{Rb}$ or Cs and $\text{X} = \text{S}, \text{Se}$ or Te . *Z Anorg Allg Chem.* **1989**, *574*, 99-106.

(43) Djieutedjeu, H.; Makongo, J. P. A.; Rotaru, A. Palasyuk, A.; Takas, N. J.; Zhou, X. Y.; Ranmohotti, K. G. S.; Spinu, L.; Uher, C.; Poudeu, P. F. P. Crystal structure, charge transport, and magnetic properties of MnSb_2Se_4 , *Eur. J. Inorg. Chem.* **2011**, *26*, 3969-3977.

(44) Matar, S. F.; Wehrich, R.; Kurowski, D.; Pfitzner, A.; Eyert, V. Electronic structure of the antiferromagnetic semiconductor MnSb_2S_4 . *Phys. Rev. B*. **2005**, *71*, 235207.

(45) Leone, P.; Doussier-Brochard, C.; Andre, G.; Moelo, Y. Magnetic properties and neutron diffraction study of two manganese sulfosalts: monoclinic MnSb_2S_4 and benavidesite ($\text{MnPb}_4\text{Sb}_6\text{S}_{14}$), *Phys. Chem. Miner.* **2008**, *35*, 201-206.

(46) Bao, J. K.; Tang, Z. T.; Jung, H. J.; Liu, J. Y.; Liu, Y.; Li, L.; Li, Y. K.; Xu, Z. A.; Feng, C. M.; Chen, H.; Chung, D. Y.; Dravid, V. P.; Cao, G. H.; Kanatzidis, M. G.

Unique [Mn₆Bi₅] Nanowires in KMn₆Bi₅: A quasi-one-dimensional antiferromagnetic metal. *J. Am. Chem. Soc.* **2018**, *140*, 4391-4400.

(47) Sheldrick, G. M. A short history of SHELX. *Acta Crystallogr. A.* **2008**, *64*, 112-22.

(48) Kresse, G.; Hafner, J. *Ab initio* molecular dynamics for liquid metals. *Phys. Rev. B.* **1993**, *47*, 558(R).

(49) Kresse, G.; Furthmüller, J. Efficiency of ab-initio total energy calculations for metals and semiconductors using a plane-wave basis set. *Comp. Mater. Sci.* **1996**, *6*, 15-50.

(50) Kresse, G.; Furthmüller, J. Efficient iterative schemes for ab initio total-energy calculations using a plane-wave basis set. *Phys. Rev. B.* **1996**, *54*, 11169.

(50) Perdew, J. P.; Burke, K.; Ernzerhof, M. Generalized gradient approximation made simple. *Phys. Rev. Lett.* **1996**, *77*, 3865-3868.

(52) Grimme, S. Semiempirical GGA-type density functional constructed with a long-range dispersion correction. *J. Comput. Chem.* **2006**, *27*, 1787-1799.

(53) Nesper, R. The Zintl-Klemm Concept - A Historical Survey. *Z. Anorg. Allg. Chem.* **2014**, *640*, 2639-2648.

(54) Tang, Z. T.; Bao, J. K.; Liu, Y.; Sun, Y. L.; Ablimit, A.; Zhai, H. F.; Jiang, H.; Feng, C. M.; Xu, Z. A.; Cao, G. H. Unconventional superconductivity in quasi-one-dimensional Rb₂Cr₃As₃. *Phys. Rev. B.* **2015**, *91*, 020506(R)

(55) Tang, Z. T.; Bao, J. K.; Wang, Z.; Bai, H.; Jiang, H.; Liu, Y.; Zhai, H. F.; Feng, C. M.; Xu, Z. A.; Cao, G. H. Superconductivity in quasi-one-dimensional Cs₂Cr₃As₃ with large interchain distance. *Sci. China Mater.* **2015**, *58*, 16-20.

(56) Johnston, D. C. The puzzle of high temperature superconductivity in layered iron pnictides and chalcogenides. *Adv. Phys.* **2010**, *59*, 803-1061.

(57) Wang, W. J.; Sun, R.; He, S. J.; Jia, Z. Y.; Su, C. L.; Li, Y.; Wang, Z. C. Atomic structure, work function and magnetism in layered single crystal VOCl. *2D Mater.*, **2021**, *8*, 015027.

(58) Goldman, A. I.; Kong, T.; Kreyszig, A.; Jesche, A.; Ramazanoglu, M.; Dennis, K.

W.; Bud'ko, S. L.; Canfield, P. C. A family of binary magnetic icosahedral quasicrystals based on rare earths and cadmium. *Nat. Mater.* **2013**, *12*, 714-718.

(59) Kong, T.; Bud'ko, S. L.; A.; Jesche, McArthur, J.; Kreyssig, A.; Goldman, A. I.; Canfield, P. C. Magnetic and transport properties of i-R-Cd icosahedral quasicrystals (R=Y, Gd-Tm). *Phys. Rev. B.* **2014**, *90*, 014424.

(60) Ibuka, S.; Iida, K.; Sato, T. J. Magnetic properties of the Ag-In-rare-earth 1/1 approximants. *J. Phys.: Condes. Matter.* **2011**, *23*, 056001.

(61) Greedan, J. E. Geometrically frustrated magnetic materials. *J. Mater. Chem.* **2001**, *11*, 37-53.

(62) Wu, P. F.; Wang, Y.; Chen, W. Z.; Hu, X. L.; Huang, B.; Xiao, Z. C. Structural and Magnetical Studies of Mixed-Valence Hexavanadate Hybrids: How Organic Ligands Affect the Magnetism of Polyoxometalates?. *Inorg. Chem.* **2021**, *60*, 4347-4351.

(63) Kunes, J.; Lukoyanov, A. V.; Anisimov, V. I.; Scalettar, R. T.; Pickett, W. E. Collapse of magnetic moment drives the Mott transition in MnO. *Nat. Mater.* **2008**, *7*, 198-202.

(64) Sato, T. J. Short-range order and spin-glass-like freezing in A-Mg-R (A = Zn or Cd; R = rare-earth elements) magnetic quasicrystals, *Acta Crystallogr. Sect. A.* **2005**, *61*, 39-50.

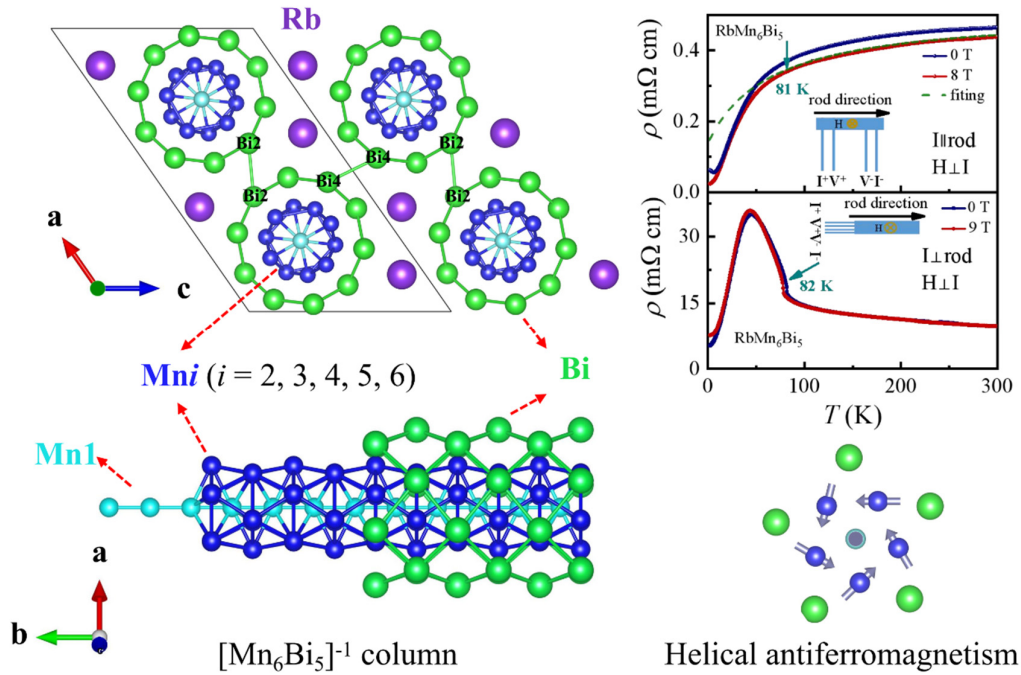
(65) Tamura, R.; Muro, Y.; Hiroto, T.; Nishimoto, K.; Takabatake, T. Long-range magnetic order in the quasicrystalline approximant Cd₆Tb. *Phys. Rev. B.* **2010**, *82*, 220201(R).

(66) Gunnarsson, O.; Calandra, M.; Han, J. E. Colloquium: Saturation of electrical resistivity. *Rev. Mod. Phys.* **2003**, *75*, 1085-1099.

(67) Valla, T.; Johnson, P. D.; Yusof, Z.; Wells, B.; Li, Q.; Loureiro, S. M.; Cava, R. J.; Mikamik, M.; Morik, Y.; Yoshimurak, M.; Sasakik, T. Coherence-incoherence and dimensional crossover in layered strongly correlated metals. *Nature.* **2002**, *417*, 627630.

(68) Miwa, H. Energy gaps and electrical resistivity associated with screw-type spin arrangements. *Prog. Theor. Phys.* **1963**, *29*, 477-493.

(69) Bud'ko, S. L.; Canfield, P. C. Rotational tuning of H_{c2} anomalies in $\text{ErNi}_2\text{B}_2\text{C}$: Angular-dependent superzone gap formation and its effect on the superconducting ground state. *Phys. Rev. B*. **2000**, *61*, 14932-14935.



Synopsis

A newly discovered manganese-based quasi-one-dimensional material RbMn_6Bi_5 featuring $[\text{Mn}_6\text{Bi}_5]^{-1}$ columns extending along the $[010]$ direction has been reported. Each $[\text{Mn}_6\text{Bi}_5]^{-1}$ column consists of three substructures from the center to the outside: the one-dimensional Mn1 atomic chain in the center, the Mn_5 tunnel built with Mni ($i = 2, 3, 4, 5$, and 6), and the outmost Bi_5 tunnel. RbMn_6Bi_5 exhibits an antiferromagnetic ordering around 82 K and a significant resistivity anisotropy, having a possible helical antiferromagnetic configuration based on density functional theory calculations.